

In-situ observation as activity descriptor enables rational design of oxygen reduction catalyst for zinc-air battery



Haoqing Ji, Mengfan Wang, Sisi Liu, He Sun, Jie Liu, Tao Qian*, Chenglin Yan

College of Energy, Key Laboratory of Advanced Carbon Materials and Wearable Energy Technologies of Jiangsu Province, Soochow University, Suzhou, 215006, China

ARTICLE INFO

Keywords:

Platinum
Oxygen reduction reaction
In-situ XRD
Zinc-air battery
All-solid-state battery

ABSTRACT

The widespread use of metal-air batteries for mobile applications will require reduced Pt loading and enhanced catalytic activity within their cathodes to drive the sluggish oxygen reduction reaction (ORR). Despite tremendous efforts, however, elegant bottom-up synthesis of practical nanomaterials remains highly challenging. Here, we propose “*in-situ* observation” as a novel descriptor to nicely bridge the adsorbates coverage and the oxygen reduction activity of Pt-based catalysts. *In-situ* X-ray powder diffraction characterization directly observed the ORR process and the evident change of the (111) peak intensity shows continuous oxygen adsorption on the catalyst surface. As expected, the catalyst exhibiting the greatest intensity change delivers the best oxygen reduction activity with a half-wave potential of 0.92 V versus reversible hydrogen electrode and an excellent bifunctional performance with a small potential difference of 0.75 V. Once assembled as the cathode catalyst, both aqueous and all-solid-state zinc-air battery illustrate high power density and superior cycling stability, holding great potential as a novel energy supply for wearable electronics. The cutting-edge *in-situ* observation is thus identified as a valid activity descriptor to guide less empirical synthesis of enhanced ORR electrocatalysts.

1. Introduction

Metal–air batteries [1], especially zinc-air batteries [2–4], constitute appealing solutions to the increasing energy demands on multiple occasions due to their high energy density, low cost, and intrinsic safety. However, as one of the essential reactions on the cathode electrode, oxygen reduction reaction (ORR) is kinetically sluggish and severely hindered the practical applications of such devices [5–7]. Therefore, it is of great importance to develop high-efficiency electrocatalysts to reduce the reaction overpotential and speed up the ORR process. To date, Pt-based alloy nanocrystals have been experimentally and theoretically reported as the most active catalysts for the ORR [8–10]. Alloying Pt with a second metal not only reduces the loading of scarce Pt metal but also optimizes its valence d-band center [11] because of the synergetic contributions of ligand, strain, and ensemble effect [12–14], leading to an improvement in catalytic activity compared with pure Pt. However, no clear correlation between the ORR activity and atomic structure has been established. As a result, current progress has still been primarily based on trial-and-error experimental approaches to maximize performance. In this regard, it is highly desirable to identify a valid descriptor that could be experimentally measured to guide less empirical synthesis of

enhanced Pt-based electrocatalysts.

Traditional activity descriptors include adsorbate binding energy [15–17], and electronic structure [18–20]. However, there are several limitations to use these properties to predict new catalysts. First, they can only be measured in ultrahigh vacuum and it's even harder to experimentally control them on metal surfaces [21]. Consequently, the proposed descriptor is only defined for catalysts following the same reaction mechanism and if the studied catalysts experience different reaction mechanism, the scaling relations change and the descriptor breaks down [22]. In addition, the properties of the catalysts are relatively complicated and may change in actual electrochemical environment [23]. Therefore, *ex-situ* characterizations usually provide incomplete and indirect information and it is crucial to establish activity descriptor under *in-situ* reaction conditions. Inspired by this challenge, numerous cutting-edge apparatuses have been widely used to *in-situ* monitor the ORR process [24–26], in which X-ray diffraction (XRD) could provide valuable insights into oxygen intermediates adsorption on the catalyst [27,28].

Herein, we conducted *in-situ* XRD studies on a series of highly dispersive PtNi_x nanoparticles with varying composition on nitrogen-doped carbon nanosheet (PtNi_x/NC) during the ORR process.

* Corresponding author.

E-mail address: tqian@suda.edu.cn (T. Qian).

<https://doi.org/10.1016/j.ensm.2020.02.002>

Received 24 December 2019; Received in revised form 21 January 2020; Accepted 3 February 2020

Available online 6 February 2020

2405-8297/© 2020 Elsevier B.V. All rights reserved.

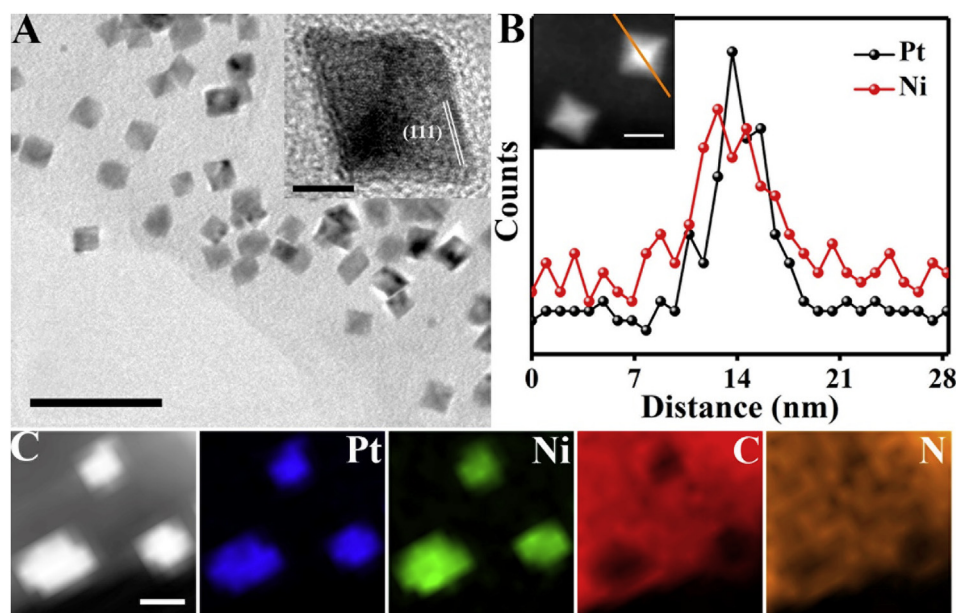


Fig. 1. (A) TEM image of PtNi_{1.3}/NC, scale bar, 10 nm. Inset: HRTEM image of PtNi_{1.3}/NC, scale bar, 5 nm. (B) Line-scan analysis (along the orange line in the inset, scale bar, 10 nm) of PtNi_{1.3}/NC. (C) HAADF-STEM image and corresponding element mappings of PtNi_{1.3}/NC. Scale bar, 10 nm. (For interpretation of the references to colour in this figure legend, the reader is referred to the Web version of this article.)

Continuous chemisorption of oxygen on the (111) surface results in evident intensity changes of the diffraction peak and a direct adsorption–activity relationship is thus obtained. As expected, the catalyst exhibiting the greatest intensity change delivers the best ORR performance with a half-wave potential ($E_{1/2}$) of 0.92 V versus reversible hydrogen electrode (vs. RHE) in 0.1 M KOH, which is 70 mV more

positive than that of the commercial Pt/C. The potential difference for bifunctional activity is as low as 0.75 V. Once assembled as the cathode catalyst, the rechargeable zinc-air battery assembled with this catalyst illustrates superior durability with 500 stable cycles. Moreover, all-solid-state battery demonstrates a high power density of 90.6 mW cm⁻², a cycling stability of 20 h, and excellent flexibility to stably light an LED

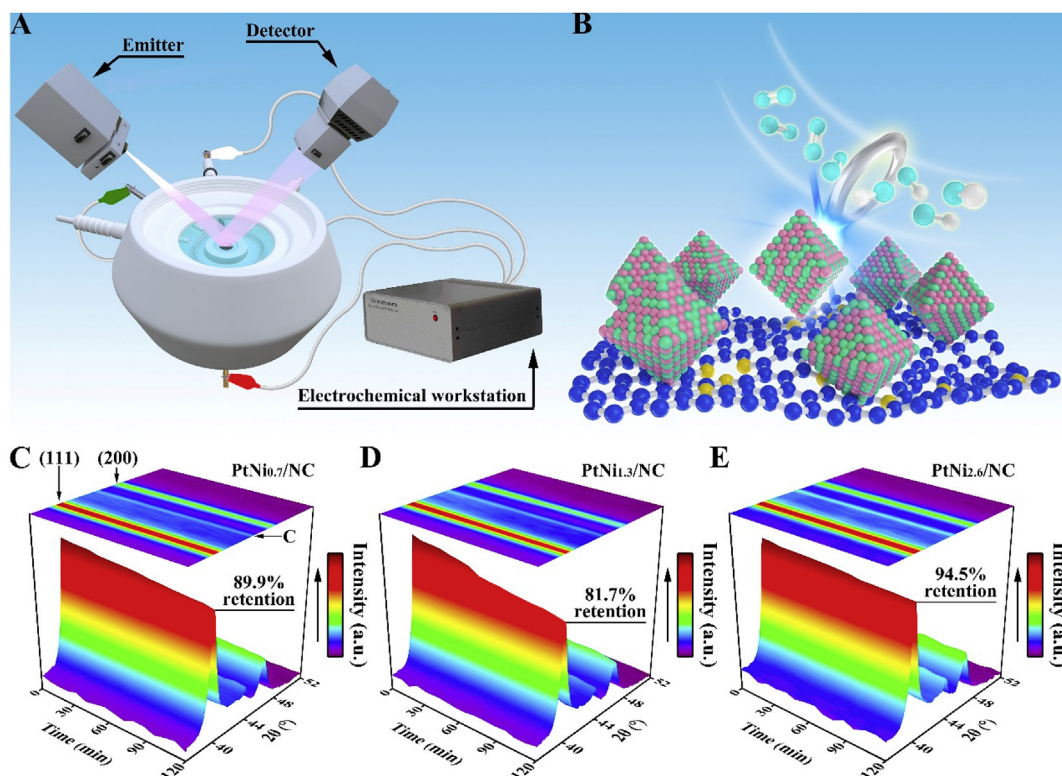


Fig. 2. *In-situ* XRD characterization. (A) Schematic diagram of the *in-situ* characterization using the home-made device. (B) Illustration of ORR process on PtNi_x/NC. The blue, yellow, green, pink, cyan, and white spheres represent C, N, Pt, Ni, O, and H atoms, respectively. Contour plots during the chronoamperometry process with (C) PtNi_{0.7}/NC, (D) PtNi_{1.3}/NC, and (E) PtNi_{2.6}/NC. (For interpretation of the references to colour in this figure legend, the reader is referred to the Web version of this article.)

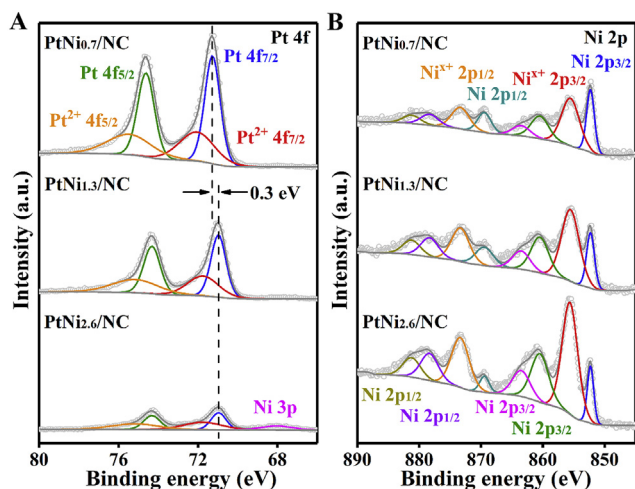


Fig. 3. Compositional analysis of the PtNi_x/NC catalysts. High resolution X-ray photoelectron spectroscopy spectrum of (A) Pt 4f and (B) Ni 2p.

bracelet when bent into a cycle.

2. Results and discussion

The proof-of-concept PtNi_x/NC were synthesized by a modified solvothermal reactions using N, N-dimethylformamide (DMF) as both reductant and solvent [29], which contained NC as a desired support. The Pt/Ni atomic ratios were varied by the addition of different amounts of Ni precursor. The specific ratios were increased from 0.7 to 1.3, and 2.6 as obtained by inductively coupled plasma mass spectrometry (ICP-MS) (Table S1). Representative transmission electron microscopy (TEM) images and high-resolution TEM (HRTEM) images (Fig. 1A, Fig. S1, and S2) clear reveal that the PtNi_x nanocrystals, which feature an octahedral shape bounded by well-defined (111) facets, are uniformly grown on the

carbon nanosheet. Pt and Ni elements are homogeneously distributed throughout the nanocrystal as suggested by the compositional line scanning profiles (Fig. 1B) and elemental mapping images (Fig. 1C). The XRD patterns of the catalysts indicate a typical face-centered cubic structure with (111), (200), and (220) crystal planes (Fig. S3). The main (111) diffractions were 40.05° for PtNi_{0.7}/NC, 40.44° for PtNi_{1.3}/NC, and 41.61° for PtNi_{2.6}/NC. Apparently, with increasing Ni composition, the (111) peak shifts to higher 2θ values, which can be attributed to the decreased lattice spacing of the cubic samples caused by the replacement of Pt atoms with smaller Ni atoms [30,31].

Since the catalytic activity is greatly dependent on the adsorption of oxygenated species on the metal surface, it would be highly desirable if such process could be monitored under *in-situ* conditions. To achieve this goal, we customized an open reaction cell (Fig. S4) and coupled it with X-ray diffractometer. An *in-situ* XRD observation during the ORR process can be realized to determine the adsorbate coverage condition on the catalyst surface (Fig. 2A and B). The chronoamperometric method was conducted to maintain continuous oxygen reduction and the recording frequency of XRD patterns was 8 min for the same position. For all three samples, two major diffractions representing (111) and (200) planes of the PtNi_x alloy can be observed (Fig. 2C–E). In great contrast to that tested under Ar (Fig. S5), with O₂ as the gas supply, the (111) peaks gradually weaken along with the ORR process, which can be attributed to the continuous chemisorption of oxygenated species that gradually blocking the diffraction signal [32]. However, different decrease extent of the (111) peak intensity can be observed for different catalysts. The intensity retention decreases in the order of PtNi_{2.6}/NC (94.5%) > PtNi_{0.7}/NC (89.9%) > PtNi_{1.3}/NC (81.7%), which means the coverage of oxygenated species increases in the order of PtNi_{2.6}/NC < PtNi_{0.7}/NC < PtNi_{1.3}/NC. With the ability to attract such abundant adsorbates on the catalyst surface, PtNi_{1.3}/NC is supposed to deliver the best ORR performance.

To clarify the adsorption origin of the PtNi_x/NC catalysts, their surface chemical environment was determined by X-ray photoelectron spectroscopy (XPS) analysis. Fig. 3A and B shows the high resolution XPS

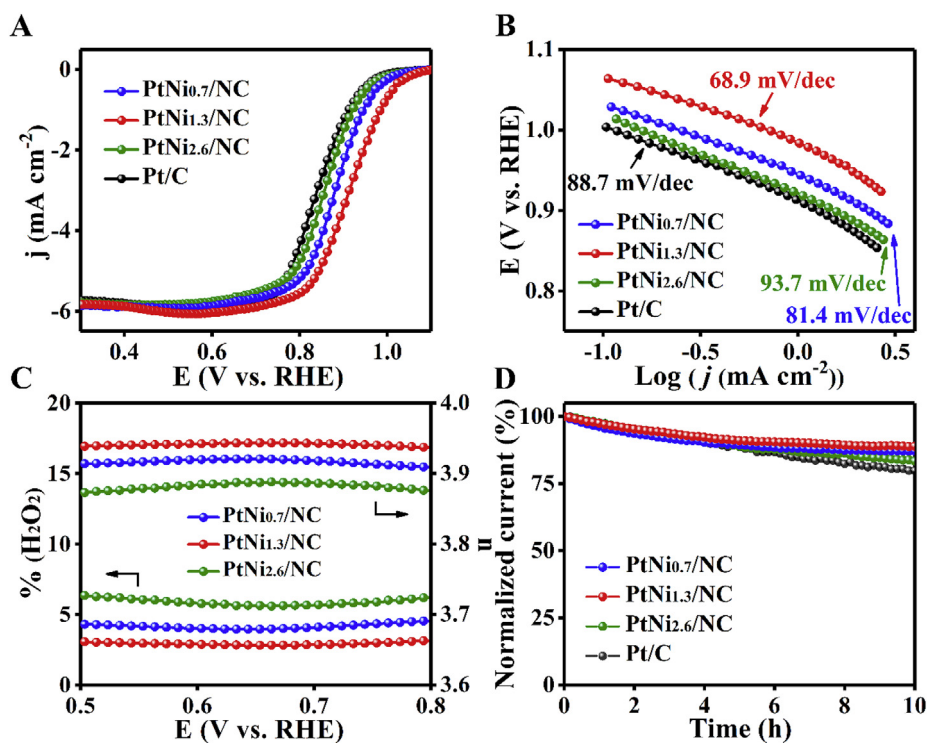


Fig. 4. Electrochemical properties of different PtNi_x/NC. (A) ORR polarization curves. (B) ORR Tafel plots derived from the corresponding LSV curves. (C) Peroxide yield and electron transfer number at various potentials. (D) ORR current-time chronoamperometric responses at 0.6 V vs. RHE of different samples.

signals for Pt 4f and Ni 2p. For all three samples, Pt shows two strong peaks corresponding to Pt 4f_{7/2} and Pt 4f_{5/2}, which can be further divided into two pairs of peaks assigned to Pt(0) and Pt(II). Along with the decrease of Pt content, the dominant composition changes from the metallic state to the oxidized state. Moreover, compared to PtNi_{0.7}/NC, the Pt 4f_{7/2} and Pt 4f_{5/2} peaks of PtNi_{1.3}/NC and PtNi_{2.6}/NC shifted from 71.32 and 74.66 eV to a lower binding energy at 71.02 and 74.36 eV, respectively, suggesting that the electron density of Pt is changed and the activated photoelectrons is hindered by the increased Ni-based species [33]. Those results indicate the decrease of active sites for ORR. As for Ni 2p, the spectra consist of metallic Ni as well as Ni oxide and hydroxides, with several satellite peaks adjacent to the main peaks. Such complex multiplet splitting can be ascribed to multielectron excitation [34]. Clearly, according to the integrated area, the higher Ni content leads to more oxidized composition. Nickel hydroxide is reported to be able to facilitate the adsorption of oxygen on the nearby Pt sites and thus enhance the ORR activity of PtNi alloy [35]. Given above considerations, from PtNi_{0.7}/NC to PtNi_{1.3}/NC to PtNi_{2.6}/NC, the number of active sites decreases while the intrinsic activity of each site improves. Once a balanced Pt/Ni ratio is achieved, great oxygen adsorption can be obtained, thus facilitating the ORR process.

The electrochemical activity of each sample was then evaluated to verify if *in-situ* observation could be used as an activity descriptor. Linear sweep voltammetry (LSV) measurements were carried out on the rotating

disk electrode (RDE) in O₂-saturated 0.1 M KOH (Fig. S6). As expected, in Fig. 4A, PtNi_{1.3}/NC exhibits the best ORR activity, with the most positive E_{1/2} of 0.92 V vs. RHE, which is 70 mV more positive than the Pt/C (0.85 V vs. RHE). As for the kinetic current density, it is 29.3 mA cm⁻² for PtNi_{1.3}/NC at 0.85 V vs. RHE, and is almost 6 times larger than the Pt/C catalyst (5.1 mA cm⁻² at 0.85 V vs. RHE) (Fig. S7). The half-wave potentials of PtNi_{0.7}/NC is 0.89 V vs. RHE while for PtNi_{2.6}/NC, it is even more negative at 0.86 V vs. RHE. The Tafel slopes were obtained from the LSV curves and PtNi_{1.3}/NC exhibits a much smaller Tafel slope of 68.9 mV/dec compared with PtNi_{0.7}/NC (81.4 mV/dec) and PtNi_{2.6}/NC (93.7 mV/dec), demonstrating its superior reaction kinetics (Fig. 4B). Such desirable property can be further verified by the electrochemical impedance spectroscopy (EIS) results (Fig. S8). The PtNi_{1.3}/NC shows the smallest semicircle diameters, indicating its fastest electron transport kinetics. Subsequently, cyclic voltammetry (CV) measurements were conducted in Ar-saturated electrolyte. The electrochemical active surface area (ECSA) of the catalysts can be determined based on the CV profiles and the specific activity of each sample can be further obtained through normalization by the ECSA (Fig. S9) [36]. The specific ECSA of the PtNi_{1.3}/NC (48.2 m² per g Pt) is close to that of commercial Pt/C (65.1 m² per g Pt) and its specific activity (0.91 mA cm⁻²) is even more than 5 times higher than that of commercial Pt/C (0.18 mA cm⁻²). Rotating ring-disk electrode (RRDE) tests were performed to study the ORR catalytic efficiency of the catalysts. For PtNi_{1.3}/NC, the peroxide yield was

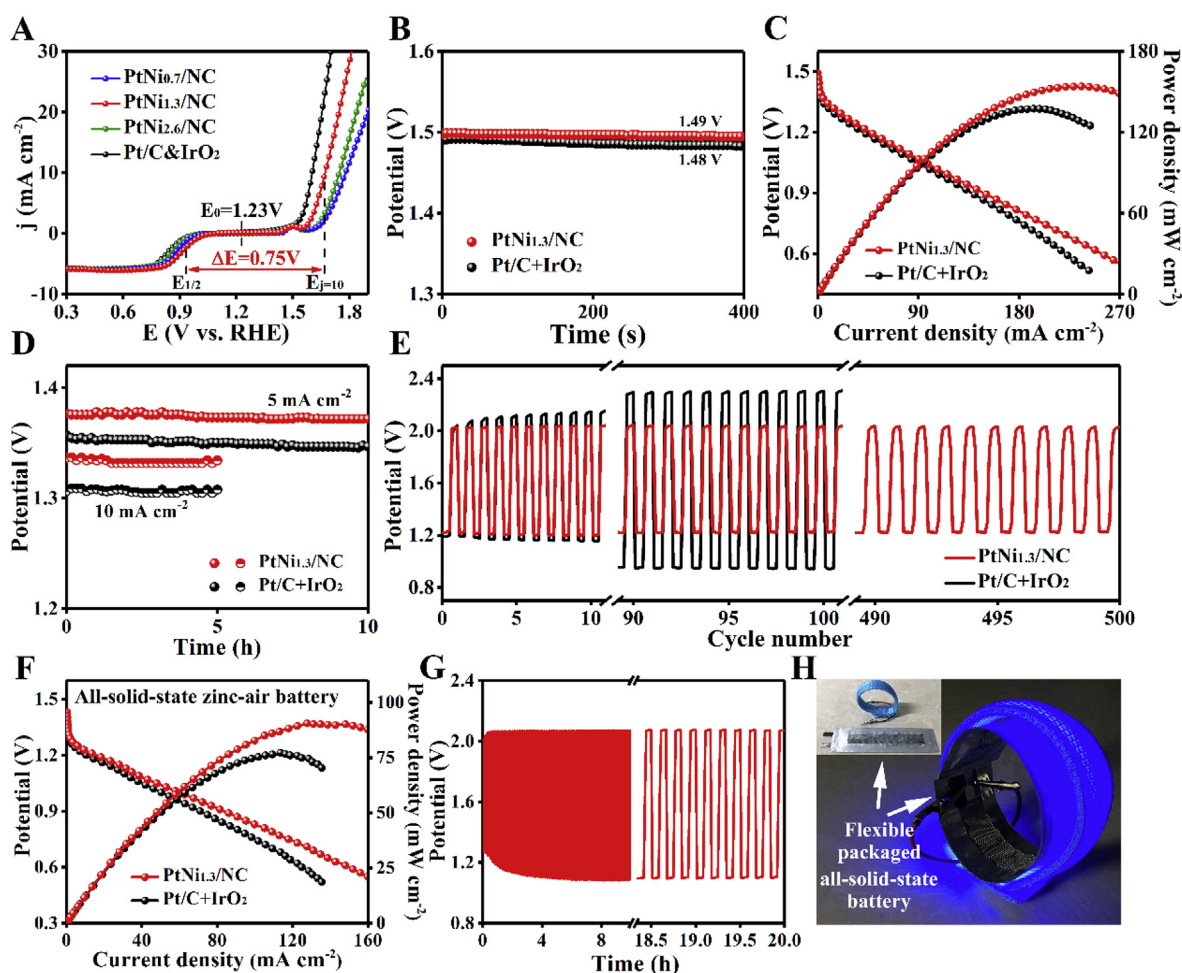


Fig. 5. Bifunctional activity of the PtNi_{1.3}/NC catalyst and its application in rechargeable zinc-air battery. (A) LSV curves of different catalysts for both ORR and OER. (B) Open-circuit plots in aqueous solution. (C) Discharge polarization curves and the corresponding power density plots. (D) Discharge curves under constant current density of 5 mA cm⁻² and 10 mA cm⁻². (E) Galvanostatic discharge and charge performance at a steady current density of 25 mA cm⁻². (F) Discharge polarization curves and the corresponding power density plots using gel electrolyte. (G) Galvanostatic discharge and charge performance using gel electrolyte. (H) Photograph of an LED bracelet powered by two all-solid-state batteries connected in series in one pack.

calculated to be below 3.2% and the electron transfer number is over 3.94 at the voltage window of 0.50–0.80 V (Fig. 4C). In addition, it also shows excellent durability in alkaline media, with only 11.1% loss of original activity after 10 h running (Fig. 4D). Apparently, the ORR activity trend among three samples is in highly agreement with the intensity change in *in-situ* observation, identifying it as a valid descriptor and nicely bridging the adsorption of oxygen and the ORR activity.

On the other hand, since Ni-based catalysts are well-known for being active phase for OER [37], the PtNi_x/NC catalysts with a certain amount of Ni hold great potential to overcome the sluggish OER kinetics as well. Inspired by the XPS results, the OER performance of different samples were also investigated. The OER polarization curves (Fig. S10A) exhibit minor peaks at around 1.5 V vs. RHE, corresponding to the oxidation of Ni(OH)₂ to NiOOH [38–40]. Such redox wave demonstrates the existence of Ni species on the surface of the catalysts, which matches well with the XPS data. Notably, instead of PtNi_{2.6}/NC, PtNi_{1.3}/NC delivers the best OER performance, requiring an overpotential of only 440 mV to achieve a current density of 10 mA cm⁻². It has been reported that only the active sites in direct contact with the conductive support are active towards OER [41]. Thus, the superior OER activity of PtNi_{1.3}/NC can be attributed to the synergistic effect between the excellent electronic conductivity of Pt phase and the high intrinsic activity of Ni species. In addition, the catalyst also exhibits desirable reaction kinetics (Fig. S10B) and durability (Fig. S11). That is, the balanced Pt/Ni ratio not only contributes to the enhanced ORR performance but also helps facilitate the OER process. The overall bifunctional activity can be evaluated by the potential gap (ΔE) between the E_{1/2} for ORR and the E_{j=10} for OER. The PtNi_{1.3}/NC shows a small ΔE of 0.75 V, which even outperforms the combination of Pt/C and IrO₂ (Fig. 5A). Moreover, careful characterizations with TEM, XRD, and XPS exhibit that the catalyst morphology, crystal parameters, and chemical state property remained unchanged after electrocatalysis (Figs. S12–S14), confirming the robustness of the PtNi_{1.3}/NC, which holds great promise to be applied in zinc-air battery.

To demonstrate the practical application of PtNi_{1.3}/NC, home-made rechargeable zinc-air battery was constructed [42,43]. With the PtNi_{1.3}/NC catalyst, the zinc-air battery delivers an open circuit potential of 1.49 V and a high power density of 154.1 mW cm⁻² (Fig. 5B and C), outperforming the noble metal counterpart. The discharge stability of the PtNi_{1.3}/NC electrode was confirmed by galvanostatic discharge measurements, in which the zinc-air batteries retain steady discharge plateaus of 1.38 V for 10 h at 5 mA cm⁻² and 1.33 V for 5 h at 10 mA cm⁻² (Fig. 5D). When assembled in rechargeable battery, the galvanostatic discharging/charging durability of PtNi_{1.3}/NC was tested by cycling the zinc-air battery. Fig. 5E exhibits a robust cycling performance of over 500 stable cycles for zinc-air battery with the PtNi_{1.3}/NC cathode, with negligible voltage gap increase as shown in the enlarged cycle diagram (Fig. S15), outperforming not only the Pt/C + IrO₂ counterpart (Fig. S16) but also most of the reported results (Table S2). All-solid-state zinc-air battery was then constructed to probe the potential utility of PtNi_{1.3}/NC in portable devices [44]. With PtNi_{1.3}/NC-loaded carbon cloth as cathode, polyvinyl alcohol as gel electrolyte, and polished zinc foil as anode, the battery delivers a stable open circuit potential of 1.42 V and a high power density of 90.6 mW cm⁻² (Figs. S17 and 5F). Moreover, readily cycling can be realized with such all-solid-state cell, with nearly constant potential plateau covering a duration of 20 h when cycled at 5 mA cm⁻², which is highly comparable to the recently reported state of the arts (Table S3). To further probe the practical application, two all-solid-state batteries were connected in series and then assembled in a battery pack. It can be bent into a cycle to light an LED bracelet (Fig. 5G), clearly indicating its great potential to be applied in wearable electronics.

3. Conclusion

In summary, by combining electrochemical measurements, *in-situ* XRD observation conducted during the ORR process was put forward as a new powerful activity descriptor, which nicely bridging the adsorption of

oxygenated species and the ORR activity. The evident intensity changes of the (111) peak of PtNi_{1.3}/NC obtained from the *in-situ* observation indicated abundant adsorbates on the catalyst surface. As expected, the catalyst exhibited a superior ORR activity with a E_{1/2} of 0.92 V vs. RHE and a desirable bifunctional activity with a ΔE of 0.75 V. Once assembled in the zinc-air battery, it illustrated excellent power density and robust cycling performance of over 500 stable cycles with negligible voltage gap increase. Further application of the PtNi_{1.3}/NC catalyst in all-solid-state zinc-air batteries exhibit great potential as a flexible energy supply for wearable electronics.

Declaration of competing interest

The authors declare that they have no known competing financial interests or personal relationships that could have appeared to influence the work reported in this paper.

CRedit authorship contribution statement

Haoqing Ji: Writing - original draft, Investigation, Data curation, Writing - original draft. **Mengfan Wang:** Writing - review & editing. **Sisi Liu:** Data curation. **He Sun:** Investigation. **Jie Liu:** Software. **Tao Qian:** Conceptualization, Methodology. **Chenglin Yan:** Supervision.

Acknowledgements

This work was supported by the National Natural Science Foundation of China [Nos. 21703149, 51622208, 51872193, and 5192500409] and Natural Science Foundation of Jiangsu Province [Nos. BK20190827 and BK20181168].

Appendix A. Supplementary data

Supplementary data to this article can be found online at <https://doi.org/10.1016/j.ensm.2020.02.002>.

Data availability

The data that support the findings of this study are available from the corresponding author upon reasonable request.

References

- [1] J.Y. Cheon, K. Kim, Y.J. Sa, S.H. Sahgong, Y. Hong, J. Woo, S.-D. Yim, H.Y. Jeong, Y. Kim, S.H. Joo, *Adv. Energy Mater.* 6 (2016) 1501794.
- [2] Y. Li, H. Dai, *Chem. Soc. Rev.* 43 (2014) 5257–5275.
- [3] H. Sun, S. Liu, M. Wang, T. Qian, J. Xiong, C. Yan, *ACS Appl. Mater. Interfaces* 11 (2019) 33054–33061.
- [4] M. Wang, T. Qian, S. Liu, J. Zhou, C. Yan, *ACS Appl. Mater. Interfaces* 9 (2017) 21216–21224.
- [5] W. Xia, A. Mahmood, Z. Liang, R. Zou, S. Guo, *Angew. Chem. Int. Ed.* 55 (2016) 2650–2676.
- [6] T. Palaniselvam, V. Kashyap, S.N. Bhang, J.-B. Baek, S. Kurungot, *Adv. Funct. Mater.* 26 (2016) 2150–2162.
- [7] S. Liu, M. Wang, T. Qian, J. Liu, C. Yan, *ACS Appl. Mater. Interfaces* 11 (2019) 20056–20063.
- [8] J. Li, H.-M. Yin, X.-B. Li, E. Okunishi, Y.-L. Shen, J. He, Z.-K. Tang, W.-X. Wang, E. Yücelen, C. Li, Y. Gong, L. Gu, S. Miao, L.-M. Liu, J. Luo, Y. Ding, *Nat. Energy* 2 (2017) 17111.
- [9] D. Wang, H.L. Xin, R. Hovden, H. Wang, Y. Yu, D.A. Muller, F.J. DiSalvo, H.D. Abruña, *Nat. Mater.* 12 (2013) 81–87.
- [10] X. Huang, Z. Zhao, L. Cao, Y. Chen, E. Zhu, Z. Lin, M. Li, A. Yan, A. Zettl, Y.M. Wang, X. Duan, T. Mueller, Y. Huang, *Science* 348 (2015) 1230–1234.
- [11] J.K. Nørskov, J. Rossmeisl, A. Logadottir, L. Lindqvist, *J. Phys. Chem. B* 108 (2004) 17886–17892.
- [12] V. Stamenkovic, B.S. Mun, K.J. J. Mayrhofer, P.N. Ross, N.M. Markovic, J. Rossmeisl, J. Greeley, J.K. Nørskov, *Angew. Chem. Int. Ed.* 45 (2006) 2897–2901.
- [13] T. Bligaard, J.K. Nørskov, *Electrochim. Acta* 52 (2007) 5512–5516.
- [14] J. Greeley, J.K. Nørskov, M. Mavrikakis, *Annu. Rev. Phys. Chem.* 53 (2002) 319–348.
- [15] I.C. Man, H.Y. Su, F. Calle-Vallejo, H.A. Hansen, J.I. Martinez, N.G. Inoglu, J. Kitchin, T.F. Jaramillo, J.K. Nørskov, J. Rossmeisl, *ChemCatChem* 3 (2011) 1159–1165.

- [16] Z. Pei, H. Li, Y. Huang, Q. Xue, Y. Huang, M. Zhu, Z. Wang, C. Zhi, *Energy Environ. Sci.* 10 (2017) 742–749.
- [17] Y. Yang, K. Mao, S. Gao, H. Huang, G. Xia, Z. Lin, P. Jiang, C. Wang, H. Wang, Q. Chen, *Adv. Mater.* 30 (2018), 1801732.
- [18] B.S. Mun, M. Watanabe, M. Rossi, V. Stamenkovic, N.M. Markovic, J.P.N. Ross, *J. Chem. Phys.* 123 (2005), 204717.
- [19] H. Sun, M. Wang, X. Du, Y. Jiao, S. Liu, T. Qian, Y. Yan, C. Liu, M. Liao, Q. Zhang, L. Meng, L. Gu, J. Xiong, C. Yan, *J. Mater. Chem.* 7 (2019) 20952–20957.
- [20] Y. Han, Y. Wang, R. Xu, W. Chen, L. Zheng, A. Han, Y. Zhu, J. Zhang, H. Zhang, J. Luo, *Energy Environ. Sci.* 11 (2018) 2348–2352.
- [21] W.T. Hong, M. Risch, K.A. Stoerzinger, A. Grimaud, J. Suntivich, Y. Shao-Horn, *Energy Environ. Sci.* 8 (2015) 1404–1427.
- [22] A. Vojvodic, F. Calle-Vallejo, W. Guo, S. Wang, A. Toftelund, F. Studt, J.I. Martinez, J. Shen, I.C. Man, J. Rossmeisl, T. Bligaard, J.K. Noorskov, F. Abild-Pedersen, *J. Chem. Phys.* 134 (2011), 244509.
- [23] X. Tuaeav, S. Rudi, V. Petkov, A. Hoell, P. Strasser, *ACS Nano* 7 (2013) 5666–5674.
- [24] Y. Ma, W. Gao, H. Shan, W. Chen, W. Shang, P. Tao, C. Song, C. Addiego, T. Deng, X. Pan, J. Wu, *Adv. Mater.* 29 (2017), 1703460.
- [25] S. Nayak, L.J. McPherson, K.A. Vincent, *Angew. Chem. Int. Ed.* 57 (2018) 12855–12858.
- [26] Q. Jia, W. Liang, M.K. Bates, P. Mani, W. Lee, Sanjeev Mukerjee, *ACS Nano* 9 (2015) 387–400.
- [27] S. Liu, M. Wang, X. Sun, N. Xu, J. Liu, Y. Wang, T. Qian, C. Yan, *Adv. Mater.* 29 (2017), 1704898.
- [28] H. Ji, M. Wang, S. Liu, H. Sun, J. Liu, T. Qian, C. Yan, *Electrochim. Acta* 334 (2020), 135562.
- [29] Q. Li, H. Zhu, L. Zheng, L. Fan, N. Wang, Y. Rong, Y. Ren, J. Chen, J. Deng, X. Xing, *Nano Lett.* 17 (2017) 7892–7896.
- [30] J. Wu, A. Gross, H. Yang, *Nano Lett.* 12 (2012) 798–802.
- [31] L. Gan, M. Heggen, S. Rudi, P. Strasser, *Nano Lett.* 11 (2011) 5423–5430.
- [32] M. Wang, W. Wang, T. Qian, S. Liu, Y. Li, Z. Hou, J.B. Goodenough, P.M. Ajayan, C. Yan, *Adv. Mater.* 31 (2019), 1803339.
- [33] P. Wang, Q. Shao, X. Cui, X. Zhu, X. Huang, *Adv. Funct. Mater.* 28 (2018), 1705918.
- [34] K.-W. Park, J.-H. Choi, B.-K. Kwon, S.-A. Lee, Y.-E. Sung, *J. Phys. Chem. B* 106 (2002) 1869–1877.
- [35] S. Fu, C. Zhu, J. Song, M.H. Engelhard, Y. He, D. Du, C. Wang, Y. Lin, *J. Mater. Chem.* 4 (2016) 8755–8761.
- [36] S. Sun, G. Zhang, D. Geng, Y. Chen, R. Li, M. Cai, X. Sun, *Angew. Chem. Int. Ed.* 50 (2011) 422–426.
- [37] L. Han, S. Dong, E. Wang, *Adv. Mater.* 28 (2016) 9266–9291.
- [38] L. Wang, H. Chen, Q. Daniel, L. Duan, B. Philippe, Y. Yang, H. Rensmo, L. Sun, *Adv. Energy Mater.* 6 (2016), 1600516.
- [39] L.J. Enman, M.S. Burke, A.S. Batchellor, S.W. Boettcher, *ACS Catal.* 6 (2016) 2416–2423.
- [40] Z. Cai, D. Zhou, M. Wang, S.-M. Bak, Y. Wu, Z. Wu, Y. Tian, X. Xiong, Y. Li, W. Liu, S. Siahrostami, Y. Kuang, X.-Q. Yang, H. Duan, Z. Feng, H. Wang, X. Sun, *Angew. Chem. Int. Ed.* 57 (2018) 9392–9396.
- [41] S. Zou, M.S. Burke, M.G. Kast, J. Fan, N. Danilovic, S.W. Boettcher, *Chem. Mater.* 27 (2015) 8011–8020.
- [42] J. Zhou, M. Wang, T. Qian, S. Liu, X. Cao, T. Yang, R. Yang, C. Yan, *Nanotechnology* 28 (2017), 365403.
- [43] M. Wang, T. Qian, J. Zhou, C. Yan, *ACS Appl. Mater. Interfaces* 9 (2017) 5213–5221.
- [44] M. Wang, S. Liu, N. Xu, T. Qian, C. Yan, *Adv. Sustainable Syst.* 1 (2017), 1700085.